Supporting Information for "A model for the formation of esker"

I. J. Hewitt[1], **T. T. Creyts**[2]

[1]Mathematical Institute, University of Oxford
[2]Lamont-Doherty Earth Observatory, Columbia University

S1 Introduction

This supplementary information provides full details of the mathematical model, as well as additional figures. It is all contained within this pdf.

The schematic illustrations from the main text are reproduced here (figure S1) for ease of reference. A list of primary variables is also included in table S1.

In section S2 we describe the plastic-ice-approximation model for the ice-sheet topography, and provide a simple parameterisation for how the melt rate m and catchment basin length ℓ_a vary with changing equilibrium line altitude (as a proxy for changing climate).

In section S3 we describe the channel model from the main text in greater detail.

In section S4 we analyse the behaviour of the boundary layer near the margin, where deposition occurs. This allows us to calculate the total deposition rate Q_D in terms of the sediment flux and water flux being delivered to the margin, and motivates the scaling in figure 4 of the main text.

Section S5 discusses the role of bed topography in altering the deposition dynamics.

Finally, in order to discuss the impact of evolving climate, we provide scaling arguments in section S6 for how the width ℓ_c of the catchment basin, and hence water flux Q_m, vary with changing melt rate. The estimates of catchment basin width follow essentially the same idea as existing arguments for subglacial channel spacing [*Boulton et al.*, 2009; *Schoof*, 2010; *Hewitt*, 2011], finding the scale over which effective pressure gradients are able to draw water laterally into a channel. The result is to suggest that when the equilibrium line altitude is higher (so there is more melting overall), the catchment basins are longer and narrower, but the water flux through each individual channel is larger.

S2 Ice-sheet topography and surface melt

The shape of the ice sheet margin during retreat is likely to have varied in time depending on underlying topography and the history of accumulation and melt. For the purposes of this study, we adopt a generic shape of the ice sheet that remains approximately constant, relative to the margin, as the margin retreats. The simplest option is the plastic ice model [*Nye*, 1952; *Weertman*, 1961], in which the horizontal shear stress in the ice is set equal to a yield stress τ_c,

$$\rho_i g h \left(\frac{\partial b}{\partial X} + \frac{\partial h}{\partial X} \right) = \tau_c, \qquad h = 0 \text{ at } X = 0. \tag{1}$$

Corresponding author: Ian Hewitt, `hewitt@maths.ox.ac.uk`

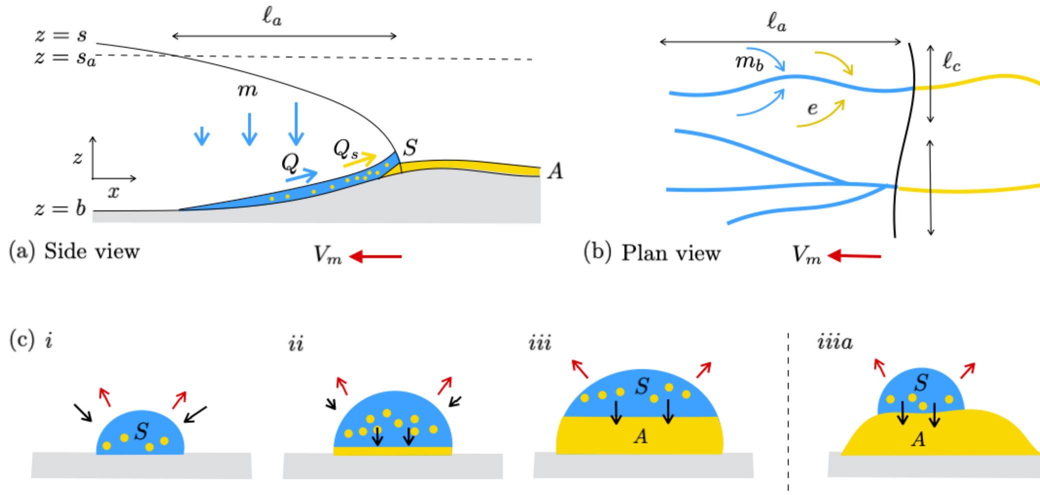

Figure S1. (a) Side and (b) plan views of the esker formation mechanism discussed in this paper. As the ice-sheet margin retreats, subglacial channels of cross-sectional area S deposit sediments near the margin, leaving behind an esker of cross-sectional area A. The size of the deposit depends on sediment supply e, melt-water supply $m + m_b$, channel spacing ℓ_c, and retreat rate V_m, all of which can vary through time. (c) Downstream evolution channel cross section. Red arrows denote wall melting. Black arrows denote creep closure and sediment deposition. (i) Far from the margin sediment flux is below the carrying capacity and the cross-sectional area S is governed by a balance between wall melting and creep closure; (ii) as the margin is approached and the channel enlarges, deposition starts to occur; (iii) at the margin a deposit of cross-sectional area A is formed and there is a balance between wall melting and deposition; (iiia) alternatively the channel may move from side to side over time, depositing sediment over a wider area (the model does not distinguish between the situations in (iii) and (iiia)).

Q	Water flux (m^3 s^{-1})
Q_s	Sediment flux (m^3 s^{-1})
Q_m	Water flux at margin (m^3 s^{-1})
$Q_{s\,m}$	Sediment flux approaching margin (m^3 s^{-1})
S	Cross-sectional area of channel (m^2)
A	Cross-sectional area of sediment (m^2)
N	Effective pressure (Pa)
$\mathcal{Q}_{eq}$	Equilibrium sediment flux (m^3 s^{-1})
V_m	Margin retreat rate (m s^{-1})
D	Deposition rate (m^2 s^{-1})
Q_D	Total (volumetric) deposition rate (m^3 s^{-1})
Ψ	Hydraulic potential gradient (Pa m^{-1})
Ψ_s	Topographic potential gradient ($N = 0$) (Pa m^{-1})
Ψ_b	Atmospheric potential gradient ($p_w = 0$) (Pa m^{-1})

Table S1. Primary variables in the model.

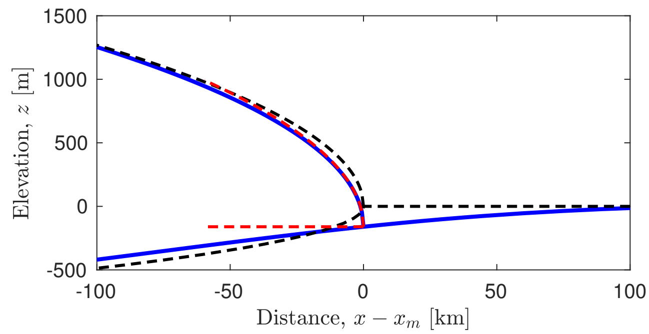

Figure S2. An isostatically depressed ice sheet margin from the solution to (1) and (2), showing bed and surface elevations. For comparison, black dashed lines show the 'Archimedean' solution with $b = -(\rho_i/\rho_m)h$, to which the solution converges in the far field, but which is not a good approximation close to the margin. Red dashed lines show the square-root approximation $b = b_0$, $h = (2\tau_c X/\rho_i g)^{1/2}$ that is used for the near-margin analysis of the subglacial channel.

Here h is the ice thickness, b is the bed topography, and X is distance backward from the margin, while ρ_i is the density of ice, and g is the gravitational acceleration.

We assume that the bed is horizontal in the absence of any ice, but account for the elastic component of isostatic depression by treating the lithosphere as an elastic sheet with bending stiffness B overlying a mantle of density ρ_m, subject to the weight of the ice sheet on top. The bed elevation therefore satisfies

$$B\frac{\partial^4 b}{\partial X^4} + \rho_m g b = -\rho_i g h, \qquad \frac{\partial^2 b}{\partial X^2},\ \frac{\partial^3 b}{\partial X^3} \to 0 \text{ as } X \to \pm\infty. \tag{2}$$

There is a natural bending length in this equation, over which the lithosphere responds to loading, $\ell_b = (B/\rho_m g)^{1/4} \approx 75$ km. The solution to (1) and (2) is shown in figure S2. The square-root profile $h = (2\tau_c X/\rho_i g)^{1/2}$ (which is the exact solution on a flat bed) is a good approximation close to the margin. This model ignores the timescale for isostatic adjustment.

The problem (1)-(2) can in fact be scaled to remove all parameters except ρ_i/ρ_m, and we find that the bed height b_0 and bed slope b_1 at the margin are

$$b_0 = -0.18\left(\frac{B}{\rho_m g}\right)^{1/8}\left(\frac{\tau_c}{\rho_i g}\right)^{1/2} \approx -164 \text{ m}, \quad b_1 = 0.18\left(\frac{\rho_m g}{B}\right)^{1/8}\left(\frac{\tau_c}{\rho_i g}\right)^{1/2} \approx 0.002, \tag{3}$$

where the first numerical factors come from the solution of the scaled problem and the second are for the specific values from Table S2.

Strictly speaking, the yield-stress balance in (1) assumes that the ice is moving in the direction of the surface slope. The ice velocity is determined from mass conservation (the ice must move in such a way as to sustain the equilibrium topography), and during margin retreat this can lead to an inconsistency. Instead, there is a stagnant region near the margin (in which the ice simply down-wastes), and the yielded region starts a short distance upstream of the margin. The stagnant region is typically small, and moreover the stress balance in (1) is not strictly appropriate all the way to the margin [*Nye*, 1967]. Therefore we will ignore this slight inconsistency and use the same shape for both stagnant and moving ice.

In discussing ice-sheet retreat, we adopt a simple estimate of melting rates and retreat rates based on a constant accumulation rate a and a surface melt rate m that varies linearly with surface elevation $s = b + h$ according to

$$m = \max\left[0, \lambda(s_a - s)\right]. \tag{4}$$

Here s_a is the elevation at which melting begins and λ is a melting lapse-rate. The equilibrium line altitude is given by $s_e = s_a - a/\lambda$, and either s_a or s_e can be viewed as controls that vary through time to parameterise climatic forcing. We expect these to vary roughly linearly with mean air temperature. Using the approximate square-root profile $s = b_0 + (2\tau_c X/\rho_i g)^{1/2}$ (see figure S2), the length of the ablation zone (where surface melting occurs) is $\ell_a = \rho_i g(s_a - b_0)^2/2\tau_c$, and the total melt rate per unit width of the ice margin is

$$M = \int_0^{\ell_a} m \,\mathrm{d}X = \frac{\rho_i g \lambda (s_a - b_0)^3}{6\tau_c}. \tag{5}$$

In terms of this total melt rate, the average surface melt over the ablation area is M/ℓ_a, and the length of the ablation zone is

$$\ell_a = \left(\frac{9\rho_i g}{2\tau_c}\right)^{1/3} \frac{M^{2/3}}{\lambda^{2/3}}. \tag{6}$$

For reference, the total melt rate M takes values on the order of 10^{-3} m^2 s^{-1}, which would correspond to an average melt rate of 1 m y^{-1} over a 30 km flow-line, and would provide a channel flux of 10 m^3 s^{-1} over a 10 km wide catchment.

Note that the total melt rate M increases roughly as the cube of the ablation altitude s_a, which itself can be expected to vary linearly with temperature. Thus the total melt rate increases strongly with increasing temperature. This is simply a consequence of the convex shape of the ice sheet which causes a large expansion in the melting area as well as an increase in melt rate everywhere.

S3 Subglacial channel dynamics

Here we recapitulate the model described in the main text, elaborating on some details and assumptions.

Water flow at the bed of the ice sheet is driven by gradients of the hydraulic potential

$$\Phi = \rho_w g b + p_w = \rho_i g h + \rho_w g b - N, \tag{7}$$

where b is the bed elevation, h is the ice thickness, and the effective pressure, $N = \rho_i g h - p_w$, is the difference between the hydrostatic ice pressure and the water pressure p_w. In addition, ρ_w is the density of water, ρ_i is the density of ice, and g is the gravitational acceleration. We split the potential gradient $\Psi = -\partial\Phi/\partial x$ into components, writing

$$\Psi = \Psi_s + \frac{\partial N}{\partial x}, \qquad \Psi_s = -\rho_i g \frac{\partial h}{\partial x} + \Psi_b, \qquad \Psi_b = -\rho_w g \frac{\partial b}{\partial x}. \tag{8}$$

Here x measures distance along the channel, which we assume to be perpendicular to the ice-sheet margin. Ψ_b would be the potential gradient for flow at atmospheric pressure along the bed ($p_w = 0$), and Ψ_s would be the potential gradient if the basal water pressure equaled the overburden ice pressure ($N = 0$).

The conservation equation for water is given by

$$\frac{\partial Q}{\partial x} = \ell_c(m_b + m), \tag{9}$$

Here Q is the water flux (discharge), x is distance along the channel, ℓ_c is the width of the channel catchment, m_b is the basal melt rate, and m is the surface melt rate, which is assumed to be delivered into the channel by a combination of moulins, crevasses and tributary channels. Wall melting and temporal changes in channel storage are insignificant to the mass balance. The discharge is related to the cross-sectional area of the channel S by a turbulent drag law, which can be written in the form [*Röthlisberger*, 1972; *Nye*, 1976; *Flowers*, 2015],

$$Q = K_c S^{5/4} \Psi^{1/2}, \tag{10}$$

where K_c is a constant. For a semi-circular cross-section and assuming a turbulent drag law $\tau = f\rho_w U^2$, with $U = Q/S$, this is given by $K_c^2 = \pi^{1/2}/2^{1/2}(\pi+2)f\rho_w$.

The equivalent conservation equation for sediment is the Exner equation,

$$(1-n_s)\frac{\partial A}{\partial t} + \frac{\partial Q_s}{\partial x} = \ell_c e, \tag{11}$$

in which Q_s is the sediment flux, A is the cross-sectional area of deposited sediments, n_s is the porosity of the deposited sediments, and e is the sediment source expressed as an average value across the catchment width ℓ_c. The sediment source e is assumed to come from the surrounding bed and is carried into the channel by inflowing water, or by melting out of the ice walls. Its magnitude is almost certainly a major control on esker formation, but for the purposes of this model we take it to be prescribed. We expect typical values on the order of 1 mm y^{-1}, based upon broad-scale estimates of glacial erosion [*Hallet et al.*, 1996; *Cowton et al.*, 2012] (which must ultimately provide the sediment supply on longer timescales).

The Exner equation serves to determine both the sediment flux Q_s and the evolution of the deposited area A. This is achieved through the constraint

$$Q_s \le \mathcal{Q}_{eq} \text{ and } A = 0, \quad \text{or} \quad Q_s = \mathcal{Q}_{eq} \text{ and } A \ge 0, \tag{12}$$

where $\mathcal{Q}_{eq}$ is the carrying capacity of the channel, discussed below. This expresses the two cases of supply- or transport- limited sediment load. In the first case, there is no sediment to pick up from the bed and the sediment flux is simply determined by the source ($\partial Q_s/\partial x = \ell_c e$). In the second case the sediment load is at capacity and the deposited area may either grow or shrink to sustain the equilibrium sediment flux. It is assumed in (12) that the original channel bed is immobile. A sediment-floored channel could be accommodated by removing the constraint that $A \ge 0$, in which case the the channel would always act at its carrying capacity and negative values of A would correspond to areas where the original channel floor has been eroded. Such an extension of the model would allow for the generation of meltwater channels and tunnel valleys, but is not pursued here.

The carrying capacity depends upon the channel width and the turbulent shear stress, which is related to the average water speed $U = Q/S$. We therefore write the equilibrium sediment flux as

$$\mathcal{Q}_{eq}(Q, S). \tag{13}$$

As a concrete example, we adopt the Meyer-Peter Müller law,

$$q_s = 8\left(\frac{\Delta\rho_s g d^3}{\rho_w}\right)^{1/2} \max\left(\frac{\tau}{\Delta\rho_s g d} - \tau_c^*, 0\right)^{3/2}, \tag{14}$$

which relates the sediment flux per unit width q_s and the turbulent shear stress τ. Here $\Delta\rho_s = \rho_s - \rho_w$ is the buoyant density of sediment relative to water, d is a representative grain diameter, and $\tau_c^* \approx 0.047$ is a critical Shields stress for sediment motion [*Meyer-Peter and Mueller*, 1948]. Using the turbulent drag parameterisation $\tau = f\rho_w U^2$, and noting that the width of the channel floor is $(8S/\pi)^{1/2}$, this gives

$$\mathcal{Q}_{eq}(Q, S) = 8\left(\frac{8\Delta\rho_s g d^3 S}{\pi\rho_w}\right)^{1/2} \max\left(\frac{f\rho_w Q^2}{\Delta\rho_s g d S^2} - \tau_c^*, 0\right)^{3/2}. \tag{15}$$

We emphasise that this particular choice of sediment flux law is not fundamental to the model and other formulations could be expressed in a similar form [e.g. *van Rijn*, 1984a,b; *Garcia and Parker*, 1991; *Beaud et al.*, 2016, 2018].

An equivalent way of expressing sediment conservation is to split into two equations, for the deposited and mobilised sediment, connected by the deposition rate D,

$$\frac{\partial Q_s}{\partial x} = \ell_c e - D, \tag{16}$$

$$\frac{\partial A}{\partial t} = \frac{D}{1-n_s}. \tag{17}$$

The deposition rate can be defined in terms of a settling length ℓ_{eq} over which Q_s adjusts to $\mathcal{Q}_{eq}$ [*Einstein*, 1968; *Phillips and Sutherland*, 1989],

$$D = \begin{cases} \frac{Q_s - \mathcal{Q}_{eq}}{\ell_{eq}} & Q_s > \mathcal{Q}_{eq} \text{ or } A > 0, \\ 0 & \text{otherwise.} \end{cases} \tag{18}$$

This formulation is more convenient for numerical computations than the complementarity statement in (12), which is equivalent to taking the limit $\ell_{eq} \to 0$. We expect ℓ_{eq} to be small compared to the length scales of interest, so view the two approaches as equivalent. Our numerical solutions make use of (18).

A slightly different method of distinguishing the different cases of transport- and supply- limited sediment dynamics is invoked by *Beaud et al.* [2018], in which an additional variable, the mobilised sediment volume, is used to allow the fraction $Q_s/\mathcal{Q}_{eq}$ to vary between 0 and 1 depending on sediment supply and the fraction of the bed that can be mobilised. There appear to be a number of different ways of treating this problem, which are to some extent complementary, but which may differ in their numerical implementation.

The final ingredient is the evolution equation for the channel cross-section, describing the processes in figure S1. This describes the competition between melt-driven opening, viscous creep-driven closure of the channel walls, and infill by deposition of sediments,

$$\frac{\partial S}{\partial t} = \frac{Q(\Psi + \beta\Psi_b)}{\rho_i \tilde{L}} - \tilde{A} S N^n - \frac{D}{1-n_s}. \tag{19}$$

The factor $\beta = \rho_w c_w \gamma/(1-\rho_w c_w \gamma)$ accounts for the pressure dependence of the melting point, where c_w is the specific heat capacity of water and γ is the Clapeyron slope, and $\tilde{L} = (1+\beta)L$ is a modified latent heat. $\tilde{A}$ parameterises ice creep, and for a semi-circular channel is given by $\tilde{A} = 2A_{\mathrm{Glen}}/n^n$ where A_{Glen} and $n \approx 3$ are the coefficient and exponent in Glen's flow law for ice.

To summarise, the full model is given by (8)-(10), (16)-(18), and (19). With given topography (b and h), melt inputs (m_b and m), and sediment input (e), the equations can be solved numerically to determine the water flux, channel cross-section, hydraulic potential, and sediment flux. All of these are coupled together, so the behaviour of the model is quite complex. The boundary conditions are that the effective pressure is zero at the margin (hydraulic potential is atmospheric, or hydrostatic in a proglacial lake), and the discharge is zero at the start of the domain (at $x - x_m = -100$ km in our examples).

We solve the model in steady state, in a frame that retreats with the ice margin. That means the time derivatives $\partial/\partial t$ are replaced by 'advective' derivatives $-V_m \partial/\partial x$. An example solution is shown in figure 3 of the main text and reproduced in figure S3 for reference. Discharge increases with distance downstream, as does the cross-sectional channel area. However, the area increases more significantly near the margin, due to thinner ice which limits creep closure. This causes the velocity of the water to reduce and

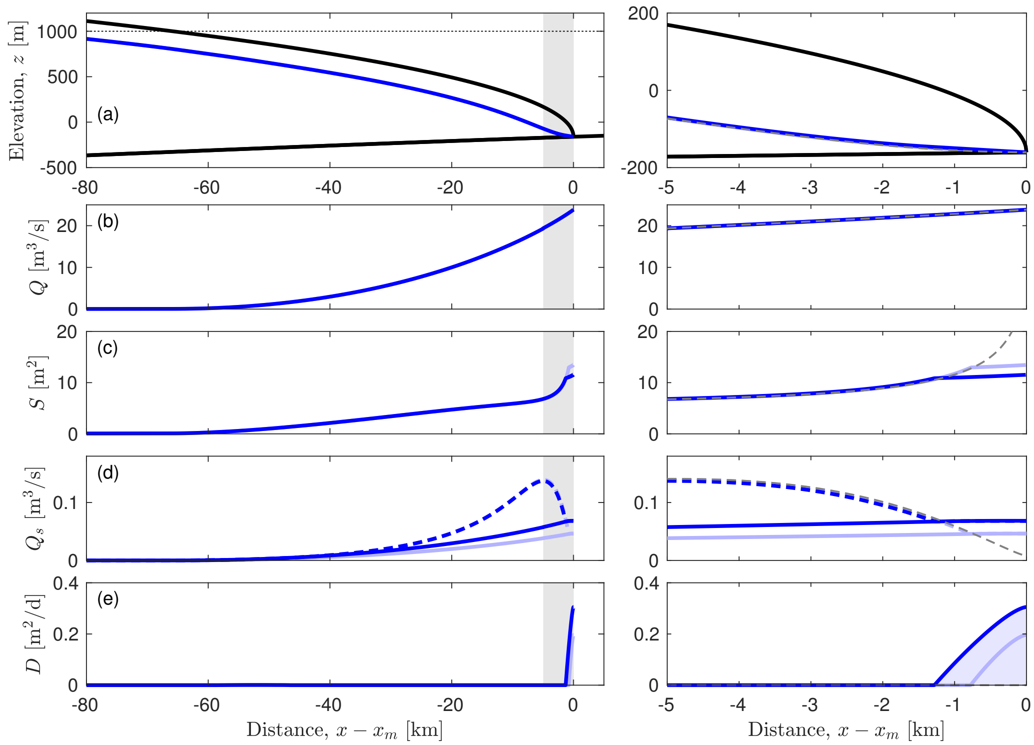

Figure S3. Steady solution to the model showing (a) hydraulic head, (b) discharge, (c) cross-sectional area, (d) sediment flux (dashed line is carrying capacity $\mathcal{Q}_{eq}$), and (e) deposition rate. Right-hand panels show an enlargement of the region near the margin. The sediment source e is proportional to the meltwater source, with $e/m = 0.003$ (darker shading) and 0.002 (lighter shading, obscured for most variables), and grey dashed lines show the equivalent solution when there is no sediment. Catchment width is $\ell_c = 10$ km, and the basal melt rate is $m_b = 5$ mm y^{-1}. Surface melt input is $m = \max(0, \lambda(s_a - s))$, where $\lambda = 3 \times 10^{-3}$ y^{-1} and $s_a = 1000$ m is the elevation below which runoff starts, indicated by the dotted line in (a). The topography is also shown in black in (a). Other parameter values are in Table S2.

ρ_w	1000 kg m^{-3}	f	0.02
ρ_i	916 kg m^{-3}	K_c	0.11 m$^{3/2}$ kg$^{-1/2}$
ρ_s	2600 kg m^{-3}	τ_c^*	0.047
ρ_m	3300 kg m^{-3}	d	1 mm
g	9.8 m s^{-2}	ℓ_{eq}	100 m
L	3.3×10^5 J kg^{-1}	n_s	0.3
β	0.46	τ_c	10^5 Pa
n	3	B	10^{24} N m
$\tilde{A}$	1.8×10^{-25} Pa^{-3} s^{-1}	λ	3 m y^{-1} km^{-1}

Table S2. Parameter values.

the carrying capacity therefore decreases as the margin is approached [*Beaud et al.*, 2018]. The usual situation is that the sediment flux is below the carrying capacity until near the margin, so deposition occurs predominantly in this region, which we refer to as a boundary layer, and which we analyse further below.

It is helpful to define the water flux and sediment flux approaching the margin. The water flux is given by

$$Q_m = \ell_c M, \qquad M = \int_{x_m - \ell_a}^{x_m} m_b + m \, \mathrm{d}x, \tag{20}$$

where M is the total melt rate per unit width of the margin, x_m is the location of the margin, and the channel length is assumed to be the same as the catchment basin length ℓ_a. We mostly ignore m_b by comparison with m (as we have done in (5) and in the main text).

Assuming no deposition upstream, the sediment flux arriving towards the margin is given simply by the integral of the sediment source along the channel (*cf.* (20)),

$$Q_{s\,m} = \ell_c E, \qquad E = \int_0^{x_m} e \, \mathrm{d}x. \tag{21}$$

It is possible, however, that this integrated sediment supply may already exceed the carrying capacity before the margin is approached and in that case $Q_{s\,m}$ is limited to the peak carrying capacity (the obvious maximum of the dashed line in figure S3(d)), which we find an expression for below. This is the case of transport-limited upstream flux, which we consider unlikely under normal conditions, since the required sediment supply would be very large.

S4 Analysis of near-margin boundary layer

The growth of the channel happens in a boundary layer roughly a few kilometres from the margin. The length scale ℓ_0 over which this occurs can be seen by balancing the terms in (8), (10), and the first two terms on the right hand side of (19), for a typical value of the margin discharge $Q_0 = Q_m$ given by (20). We assume the plastic scaling for the ice thickness $h_0 = \sqrt{\tau_c/\rho_i g}\,\ell_0^{1/2}$, and find that suitable scalings for the other variables are

$$\Psi_0 = \left(\frac{\tau_c \rho_i g}{\ell_0}\right)^{1/2}, \quad N_0 = \Psi_0 \ell_0, \qquad t_0 = \frac{1}{\tilde{A} N_0^n}, \qquad S_0 = \left(\frac{Q_0}{K_c \Psi_0^{1/2}}\right)^{4/5}, \quad D_0 = \frac{Q_{s0}}{\ell_0}, \tag{22}$$

and

$$\ell_0 = \left(\frac{K_c^{4/5}}{\rho_i \tilde{L} \tilde{A}}\right)^{10/(5n+7)} \frac{Q_0^{2/(5n+7)}}{(\tau_c \rho_i g)^{(5n-7)/(5n+7)}}, \qquad Q_{s0} = \frac{8 f^{3/2} \rho_w}{\Delta \rho_s g} \left(\frac{8}{\pi}\right)^{1/2} \frac{Q_0^3}{S_0^{5/2}}. \tag{23}$$

The ugly exponents are the result of the non-linearities in the turbulent drag law (10) and the flow law for ice. Using the values in Table S2, together with a typical flux $Q_0 = 10$ m^3 s^{-1}, these are

$$\Psi_0 \approx 370 \text{ Pa m}^{-1} \quad S_0 \approx 3.4 \text{ m}^2 \quad N_0 \approx 2.4 \text{ MPa} \quad t_0 \approx 5 \text{ d} \quad \ell_0 \approx 6.4 \text{ km} \quad Q_{s0} \approx 0.1 \text{ m}^3 \text{ s}^{-1}. \tag{24}$$

To examine this boundary layer in more detail we write $X = x_m(t) - x$ as the distance backwards from the margin $x_m(t)$, where $V_m = -\dot{x}_m$ is the margin retreat rate. Within this region, the water and sediment source terms are negligible, so the water flux Q_m is treated as constant (it is not exactly constant, as seen in figure S3b, but this is a reasonable approximation). After adopting the scalings above, the boundary layer is governed by the dimensionless equations

$$\frac{\partial N}{\partial X} = \Psi_s - \frac{1}{S^{5/2}}, \qquad -\hat{V}\frac{\partial S}{\partial X} + \mu D = \frac{1}{S^{5/2}} + \beta \Psi_b - S N^n, \qquad \frac{\partial Q_s}{\partial X} = D, \tag{25}$$

where $\hat{V} = V_m t_0/\ell_0$ is the dimensionless retreat rate (typically very small), and

$$\mu = \frac{Q_{s0} \rho_i \tilde{L}}{(1-n_s) Q_0 \Psi_0 \ell_0} \approx 3.4\, Q_m^{-1/11} \tag{26}$$

is a measure of the importance of deposition as compared with melting in the kinematics of the channel. This numerical value corresponds to the parameters in Table S2 with Q_m expressed in m^3 s^{-1}; since the exponent of Q_m is rather small, μ takes a value around 1 for a broad range of conditions.

The solution depends on the topography of the ice margin through Ψ_s and Ψ_b. We use the approximate plastic ice solution from figure S2 in which $b = b_0$ is constant and $h = \sqrt{\tau_c/\rho_i g}\,(x_m - x)^{1/2}$. When translated into the scaled coordinates this means $\Psi_s = (2X)^{-1/2}$ and $\Psi_b = 0$. We note that the qualitative behaviour of the boundary layer is the same for any choice of topography with h tending to zero at the margin, although the effect of non-zero bedslope is discussed later.

The boundary layer equations (25) are to be solved with $N = 0$ at $X = 0$, and with far-field matching conditions $S \sim \Psi_s^{-2/5}$, $N \sim \Psi_s^{7/5n}$ as $X \to \infty$. These latter conditions are appropriate to match with the solution further back under the ice sheet. We also have the far-field condition $Q_s \to Q_{s\,m}$, given by (21), and assume that this is below the equilibrium load $\mathcal{Q}_{eq}$ at large X. Recall that in the equilibrium limit $\ell_{eq} \to 0$, we either have $Q_s < \mathcal{Q}_{eq}$, in which case $D = 0$, or we have $Q_s = \mathcal{Q}_{eq}$, in which case the final equation in (25) determines D. The dimensionless carrying capacity $\mathcal{Q}_{eq}$ is given by the scaled version of (27), which is

$$\mathcal{Q}_{eq} = S^{1/2} \max\left(1/S^2 - \hat{\tau}_c, 0\right)^{3/2}, \tag{27}$$

where $\hat{\tau}_c = \tau_c^* \Delta \rho_s g d S_0^2 / f \rho_w Q_0^2 \approx 0.004$ is the rescaled critical Shields stress. The fact that this is small indicates that the turbulent shear stress in the channel is typically well above the critical stress for mobilisation. As the margin is approached and $\mathcal{Q}_{eq}(S)$ decreases, there is a point X_D at which

$$\mathcal{Q}_{eq}(S) = Q_{s\,m}, \tag{28}$$

after which deposition starts to occur. We can therefore write

$$D = \begin{cases} 0 & X > X_D, \\ \frac{\partial \mathcal{Q}_{eq}}{\partial S} \frac{\partial S}{\partial X} & X \leq X_D. \end{cases} \tag{29}$$

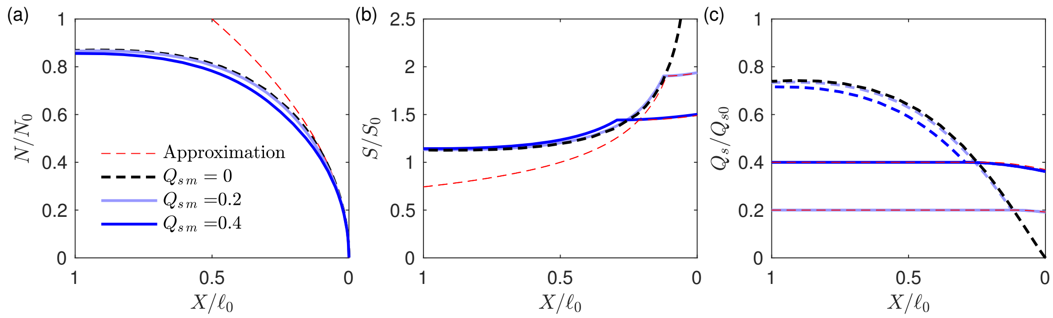

Figure S4. (a,b,c) Solutions for the near-margin boundary layer with deposition governed by (25), shown for $Q_{s\,m} = 0.2$ (lighter blue shading) and 0.4 (darker blue shading). Black dashed lines show the solution with $Q_{s\,m} = 0$ (*i.e.* no sediment), and the red dashed lines show the approximation described by (34). The solid blue line in (c) is Q_s and the dashed line is $\mathcal{Q}_{eq}$. The other parameters are $\mu = 1.6$, $\hat{\tau}_c = 0$ and $\hat{V} = 0$.

(There is a technicality here since the boundary-layer approximation of $\mathcal{Q}_{eq}$ actually decreases to zero at large X; this is an artefact of treating Q as constant and the problem is avoided by starting the boundary layer at 'large' but not infinite X).

Solutions to (25) are shown in figure S4 for two different values of upstream sediment flux, and compared to a solution with no sediment. These solutions show how deposition acts to limit the growth of the channel towards the margin (as also seen in figure S3d). As a result of this choking effect we find that the maximum possible sediment flux (the peak of the dashed line in figure S4(c)) is

$$Q_{s\,\max} = 0.65\, Q_{s0} \approx 0.007\, Q_m^{21/22}. \tag{30}$$

This is the largest possible value of the upstream sediment flux $Q_{s\,m}$. If the integrated source (21) is larger than this it indicates that the upstream channel is transport- rather than supply-limited.

The total (volumetric) rate of deposition is

$$Q_D = \int_0^\infty D \, \mathrm{d}X = Q_{s\,m} - Q_s(X = 0), \tag{31}$$

that is, the difference in sediment flux between upstream and the mouth of the channel. This is calculated numerically for different dimensionless $Q_{s\,m}$ and shown in figure S5. Unsurprisingly, this deposition rate increases with the sediment supply $Q_{s\,m}$; perhaps less obviously, the fraction of $Q_{s\,m}$ that is deposited also increases. This fraction is always considerably less than 1, indicating that a large fraction of the sediment supply is carried out to the proglacial environment.

Finally, we note that the Exner equation (11) in the boundary layer becomes (dimensionally)

$$(1 - n_s) V_m \frac{\partial A}{\partial X} + \frac{\partial Q_s}{\partial X} = 0, \tag{32}$$

assuming a steady rate of retreat. Integrating over the boundary layer gives the area of the deposit at the channel mouth,

$$A(X = 0) = \frac{Q_D}{(1 - n_s) V_m}. \tag{33}$$

This simply reflects that the size of the final deposit is determined by the total deposition rate and the amount of time that deposition has been occurring.

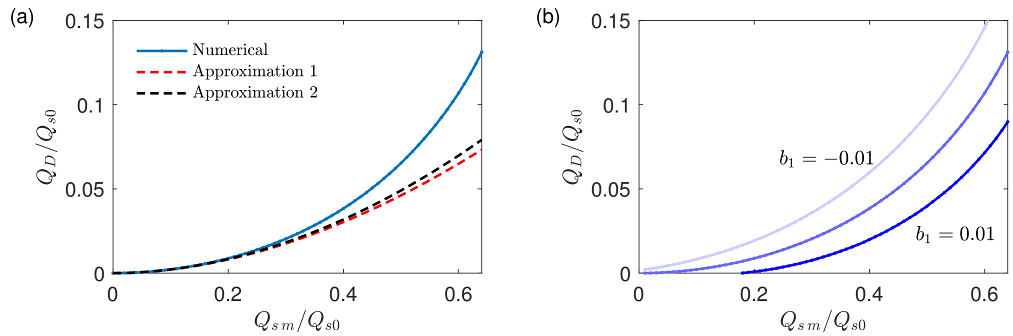

Figure S5. (a) Total deposition rate Q_D for varying upstream sediment supply $Q_{s\,m}$, obtained from the solution for the near-margin boundary layer (25). Red dashed line shows the approximation described by (34), and the black dashed line shows (35). Parameters are $\mu = 1.6$, $\hat{\tau}_c = 0$ and $\hat{V} = 0$, and the deposition rates are scaled with the sediment flux scale in (23). (b) Total deposition rate for bed slope $b_1 = -0.01$ (downwards in direction of flow), 0 and 0.01 (upwards), obtained from solving (25) with Ψ_b from (36) and $\beta\sigma = 12$.

A reasonable approximation for the dynamics of the boundary layer is obtained if we approximate the effective pressure by its limiting behaviour $N \approx (2X)^{1/2}$ (this corresponds to the hydraulic potential being approximately atmospheric near the margin). We also take $\hat{V} = \hat{\tau}_c = 0$. Until deposition starts, the balance of melting and creep closure gives $S = N^{-2n/7} \approx (2X)^{-n/7}$. Therefore $\mathcal{Q}_{eq}(S) = S^{-5/2} \approx (2X)^{5n/14}$, so we have deposition starting at $X_D \approx Q_{s\,m}^{14/5n}/2$. This leaves an ordinary differential equation for the cross-sectional area in the depositional region,

$$-\frac{5\mu}{2}\frac{1}{S^{7/2}}\frac{\partial S}{\partial X} = \frac{1}{S^{5/2}} - S(2X)^{n/2}, \tag{34}$$

to be solved backward from $X = X_D$ where $S = (2X_D)^{-n/7}$ to $X = 0$. A happy coincidence of exponents means this equation can be solved analytically, though the resulting formula is unilluminating. This approximate solution is included in figure S4 and figure S5. It is particularly valid for small sediment flux $Q_{s\,m}$, and expanding the solution for small $Q_{s\,m}$ we can derive a useful expression for the total deposition rate,

$$Q_D \approx \mathcal{C}\, Q_m^{-4/5}\, Q_{s\,m}^{29/15}, \qquad \mathcal{C} = \frac{3}{10}\left(\frac{\pi^{1/2}\Delta\rho_s g}{(8f)^{3/2}\rho_w}\right)^{29/15}\frac{(1-n_s)(\rho_i \tilde{L} K_c^2)^{-5/3}}{\tilde{A}^{2/3}\rho_i g \tau_c}, \tag{35}$$

where we have specialised to the case $n = 3$, and converted the expression to dimensional quantities, with $\mathcal{C} \approx 5.6\ \mathrm{s}^{2/15}\ \mathrm{m}^{-2/5}$ using the values in Table S2. This expression implies that the deposition rate increases approximately quadratically with sediment supply $Q_{s\,m}$, but decreases approximately linearly with water flux Q_m. The expression (35) is given in the main text, where it is compared in figure 4 to the full numerical solutions for a wide range of conditions.

S5 The role of bed topography

To investigate the effect of bed topography and pressure melting, we also solve the boundary layer model (25) with both positive and negative bed slopes. These enter through the term $\beta\Psi_b$ in (25). In dimensionless form, we have

$$\Psi_b = -\sigma b_1, \qquad \sigma = \frac{\rho_w}{\rho_i}\left(\frac{\rho_i g \ell_0}{\tau_c}\right)^{1/2} \approx 23.6\, Q_m^{1/22}, \tag{36}$$

where b_1 is the bed slope (positive for an upslope in the direction of water flow), and Q_m is expressed in $\mathrm{m}^3\ \mathrm{s}^{-1}$.

Solutions to the boundary layer model (25) with non-zero bed slope give rise to the deposition rates shown in figure S5(b). Deposition is reduced when the bed at the margin slopes upwards, and increased when the bed slopes downwards. When the bed slope is positive, the rate of viscous dissipation increases in order to compensate for the reduced efficiency of wall melting, which is still required in order to counteract both creep closure and deposition. This means that the potential gradient is increased (relative to what occurs on a flat bed) which keeps the water moving faster and therefore reduces the amount of deposition (relative to a flat bed). For low sediment loads there may be no deposition at all. Conversely, when the bed slopes downwards, the potential gradient is reduced and this leads to greater deposition. It is possible that the channel reaches atmospheric pressure upstream of the margin and becomes partially air-filled in this case.

S6 Channel spacing

The location of subglacial channels may in some cases be controlled by topography or by the location of moulins, but we concentrate on situtations where there is little underlying topography and we assume that moulins are spaced sufficiently close together that the surface water input can be treated as distributed. (Moulin density in the ablation area of the present-day Greenland ice sheet is estimated at between $0-0.88\ \mathrm{km}^{-2}$ [*Colgan and Steffen*, 2009]). In this case, we expect that the internal dynamics of the subglacial drainage system are largely responsible for the spacing of channels.

Scaling arguments for the spacing of channels have been given previously by *Boulton et al.* [2009], *Schoof* [2010] and *Hewitt* [2011]. These are slightly different but all essentially boil down to establishing the distance over which water can be drawn laterally into a channel by the water pressure difference between the channel and inter-channel watershed.

We treat the inter-channel region of the subglacial system as a porous layer with transmissivity T (transmissivity is related to permeability k and effective layer depth d by $T = \rho_w gkd/\eta_w$; an effective transmissivity can be associated with, for instance, flow through porous sediments, or linked cavities). Steady-state water conservation requires

$$\frac{\partial}{\partial x}\left(\frac{T}{\rho_w g}\Psi\right) + \frac{\partial}{\partial y}\left(\frac{T}{\rho_w g}\frac{\partial N}{\partial y}\right) = m_b + m, \tag{37}$$

where x and y are the directions parallel and transverse to the the potential gradient Ψ, and $m_b{+}m$ is the melt supply. The integral of this equation over the width of the catchment basin gives the source term in (9).

Our estimate of channel spacing comes from the balance of lateral flow with the surface melt supply m, suggesting

$$\ell_c \sim \left(\frac{TN}{\rho_w g m}\right)^{1/2}. \tag{38}$$

If we suppose the relevant pressure is the effective pressure in the channel, it can be related to the potential gradient and water flux by the balance of terms in (10) and (19),

$$N \sim \frac{K_c^{4/5n}}{(\rho_i \tilde{L}\tilde{A})^{1/n}}\Psi_s^{7/5n}Q^{1/5n}. \tag{39}$$

Then noting that the channel flux is given by $Q \sim \ell_c M$, and taking $m \sim M/\ell_a$, where ℓ_a is the length of the channel given by (6), as well as $\Psi_s \sim (\tau_c/2\rho_i g\ell_a)^{1/2}$, we can combine these ingredients to obtain a scaling estimate for the spacing as

$$\ell_c \sim \mathcal{B}\, M^{-(5n+4)/(30n-3)}, \qquad \mathcal{B} = \left[\frac{T K_c^{4/5n}}{\rho_w g (\rho_i \tilde{L}\tilde{A})^{1/n}} \left(\frac{\rho_i g}{\tau_c \lambda^2} \right)^{(5n-14)/15n} \frac{(9/2)^{1/3}}{(6\lambda^3)^{7/15n}} \right]^{5n/(10n-1)}. \tag{40}$$

Using the values in Table S2, and $Q_m = \ell_c M$, this gives

$$\ell_c \sim \mathcal{B}\, M^{-19/87}, \qquad Q_m \sim \mathcal{B}\, M^{68/87}. \tag{41}$$

According to this argument a larger melting rate M leads to larger channels, extending further from the margin, but spaced more closely together.

The actual magnitude of the spacing depends on the value taken for the transmissivity. This is highly uncertain, and may have varied significantly in time and space depending on the nature of the distributed drainage system (permeable sediments vs. linked cavities, for example) [*Boulton et al.*, 2009; *Hewitt*, 2011]. A range of values $T = 10^4$–10^8 m^2 y^{-1} together with parameters from Table S2, give $\mathcal{B} \approx 30$–3000 m$^{125/87}$ s$^{-19/87}$, and for a typical value of $M = 10^{-3}$ m^2 s^{-1} this gives a large range of estimates, $\ell_c \approx$ 120 m–14 km. Observed esker spacing suggests that the larger end of this range may be more appropriate [*Storrar et al.*, 2014].

References

Beaud, F., G. E. Flowers, and J. G. Venditti (2016), Efficacy of bedrock erosion by subglacial water flow, *Earth Surface Dynamics*, *4*(1), 125–145.

Beaud, F., G. Flowers, and J. Venditti (2018), Modeling sediment transport in ice-walled subglacial channels and its implications for esker formation and proglacial sediment yields, *Journal of Geophysical Research: Earth Surface*, *123*, 3206–3227, doi:10.1029/2018JF004779.

Boulton, G. S., M. Hagdorn, P. B. Maillot, and S. Zatsepin (2009), Drainage beneath ice sheets: groundwater–channel coupling, and the origin of esker systems from former ice sheets, *Quaternary Science Reviews*, *28*(7), 621–638.

Colgan, W., and K. Steffen (2009), Modelling the spatial distribution of moulins near Jakobshavn, Greenland, in *IOP Conference Series: Earth and Environmental Science*, vol. 6, p. 012022, IOP Publishing.

Cowton, T., P. Nienow, I. Bartholomew, A. Sole, and D. Mair (2012), Rapid erosion beneath the Greenland ice sheet, *Geology*, *40*, 343–346, doi:10.1130/G32687.1.

Einstein, H. A. (1968), Deposition of suspended particles in a gravel bed, *J. Hydraul. Div. Am. Soc. Civ. Eng.*, *95*, 1197–1205.

Flowers, G. E. (2015), Modelling water flow under glaciers and ice sheets, *Proceedings of the Royal Society A: Mathematical, Physical and Engineering Sciences*, *471*(2176), 20140,907.

Garcia, M., and G. Parker (1991), Entrainment of bed sediment into suspension, *J. Hydraul. Eng.*, *117*(4), 414–435.

Hallet, B., L. Hunter, and J. Bogen (1996), Rates of erosion and sediment evacuation by glaciers: a review of field data and their implications, *Global Planet. Change*, *12*, 213–225.

Hewitt, I. J. (2011), Modelling distributed and channelized subglacial drainage: the spacing of channels, *J. Glaciol.*, *57*, 302–314.

Meyer-Peter, E., and R. Mueller (1948), Formulas for bed load transport, *Proceedings of 2nd meeting of the International Association for Hydraulic Structures Research, Delft, 7 June 1948*, pp. 39–64.

Nye, J. (1952), A method of calculating the thickness of ice sheets, *Nature*, *169*, 529–530.

Nye, J. F. (1967), Plasticity solution for a glacier snout, *J. Glaciol.*, *6*, 695–715.

Nye, J. F. (1976), Water flow in glaciers: Jökulhlaups, tunnels and veins, *J. Glaciol.*, *17*, 181–207.

Phillips, B. C., and A. J. Sutherland (1989), Spatial lag effects in bed load sediment transport, *J. Hydraul. Res.*, *27*, 115–203.

Röthlisberger, H. (1972), Water pressure in intra- and subglacial channels, *J. Glaciol.*, *11*, 177–203.

Schoof, C. (2010), Ice-sheet acceleration driven by melt supply variability, *Nature*, *468*, 803–806.

Storrar, R. D., C. R. Stokes, and D. J. A. Evans (2014), Increased channelization of subglacial drainage during deglaciation of the Laurentide Ice Sheet, *Geology*, *42*, 239–242, doi:10.1130/G35092.1.

van Rijn, L. C. (1984a), Sediment Transport, Part I: Bed Load Transport, *J. Hydraul. Eng.*, *110*, 1431–1456.

van Rijn, L. C. (1984b), Sediment Transport, Part II: Suspended Load Transport, *J. Hydraul. Eng.*, *110*, 1613–1641.

Weertman, J. (1961), Stability of ice-age ice sheets, *J. Geophys. Res.*, *66*, 3783–3792.